Scientific Research Publishing

Optics and Photonics Journal, 2017, 7, 116-126
http://www.scirp.org/journal/opj
ISSN Online: 2160-889X
ISSN Print: 2160-8881

Design of 1.33 μm and 1.55 μm Wavelengths Quantum Cascade Photodetector

S. Khosravi[1], A. Rostami[1,2]

[1]Photonics and Nanocrystal Research Lab. (PNRL), Faculty of Electrical and Computer Engineering, University of Tabriz, Tabriz, Iran
[2]SP-EPT Labs., Industrial Park of Advanced Technologies, Tabriz, Iran

Email: skhosravi@tabrizu.ac.ir

How to cite this paper: Khosravi, S. and Rostami, A. (2017) Design of 1.33 μm and 1.55 μm Wavelengths Quantum Cascade Photodetector. *Optics and Photonics Journal*, **7**, 116-126.
https://doi.org/10.4236/opj.2017.78B016

Received: June 9, 2017
Accepted: August 7, 2017
Published: August 10, 2017

Abstract

In this paper, a quantum cascade photodetector based on intersubband transitions in quantum wells with ability of detecting 1.33 μm and 1.55 μm wavelengths in two individual current paths is introduced. Multi quantum wells structures based on III-Nitride materials due to their large band gaps are used. In order to calculate the photodetector parameters, wave functions and energy levels are obtained by solving 1-D Schrodinger–Poisson equation self consistently at 80 ˚K. Responsivity values are about 22 mA/W and 18.75 mA/W for detecting of 1.33 μm and 1.55 μm wavelengths, respectively. Detectivity values are calculated as 1.17 × 107 (Jones) and 2.41 × 107 (Jones) at wavelengths of 1.33 μm and 1.55 μm wavelengths, respectively.

Keywords

Quantum Cascade Photodetector, III-Nitride Multi Quantum Well, Responsivity and Detectivity

1. Introduction

Quantum well infrared photodetectors (QWIPs) as thermal imagers using focal plane arrays (FPAs) have been studied extensively [1] [2] [3]. For electronic transport QWIPs operate at photoconductive and photovoltaics modes. Applications of QWIPs at photoconductive mode are limited at low temperature because of existence an external applied bias. QWIPs based on photovoltaic mode are promising devices operating in high temperature and longer wavelength applications because of having no external voltage bias and dark current [4]. Quantum cascade detectors (QCDs) operating in photovoltaics mode are promising devices for small pixel large area FPAs, multicolor detection and demultip-

lexers [5]. A typical QCD consist of an active region constructed of multiple periods, each containing a thick, highly doped active QW and a nominally undoped extraction cascade composed of thinner QWs. The electrons in the ground state of doped wells in each period are excited to the upper level, then extract from this well by emission of an optical phonon. The speed of detectors based on intersubband transition (ISBT) is limited by the electron ISBT scattering time is about 1 ps [3]. Conduction-band ISBT QCDs operate based on photon–electron interactions between quantized subbands in the conduction band of wells. In QCD structure Multi quantum wells (MQWs) are designed dependant on detected wavelengths [6] [7] [8] [9] [10]. For small wavelength, quantum well structures with small conduction band offset such as GaAs/AlGaAs and InGaAs/InAlAs are used [5] [6] [7]. MQWs based on III-Nitride materials due to large conduction band offset and large LO-phonon energy are the best candidate for design of UV and NIR photodetector [11] [12] [13] [14] [15]. In the other hand, 1.33 μm and 1.55 μm wavelengths are interest, because of their importance in optical fiber communications. Attenuation of fiber glass at 1.55 μm wavelength is minimal so, this wavelength useful for long distance communication. Also, distortion of optical signal centered at 1.33 μm wavelength is minimal.

In this paper, a QCD for detecting of 1.33 μm and 1.55 μm wavelengths in individual current paths based on intersubband transitions in AlGaN/AlN MQWs is designed. Paths are separated by 100 Å AlN In order to calculate photodetector parameters, wave functions and energy levels are obtained by solving 1-D Schrodinger–Poisson equation self consistently at 80˚K. Incident wavelength excite the electrons populated the first energy level of n+ doped QWs, after that they are extracted from first wells by emitting optical phonons emission having energy close to GaN LO-phonon energy (92 meV). Responsivity of paths is about 22 mA/W and 18.75 mA/W for detecting of 1.33 μm and 1.55 μm wavelengths respectively. Detectivity values are calculated as 1.17×10^7 (Jones) and 2.41×10^7 (Jones) at wavelengths of 1.33 μm and 1.55 μm respectively.

2. Theoretical Background and Simulation Results

A 3D view of the design QCD with ability of detection 1.33 μm and 1.55 μm wavelengths in two separated paths is indicated in **Figure 1**.

Each path separated by 100 Å AlN. Paths 1 and 2 are designed for detection of 1.33 μm and 1.55 μm wavelengths, respectively. They possess 20 periods $Al_xGa_{1-x}N$/AlN MQWs, the thickness of barriers and wells listed in **Table 1** and **Table 2**. The first QWs in each path are n+ doped with concentration of 5×10^{11} cm^{-2}. Conduction band edge and wave functions for each path are shown in **Figure 2**. As shown in **Figure 2**, by incoming radiation, the photoexcited electrons transport to the lower energy levels with optical phonons emission close to GaN LO-phonon energy (92 meV) until reach the first levels in the next period of the path.

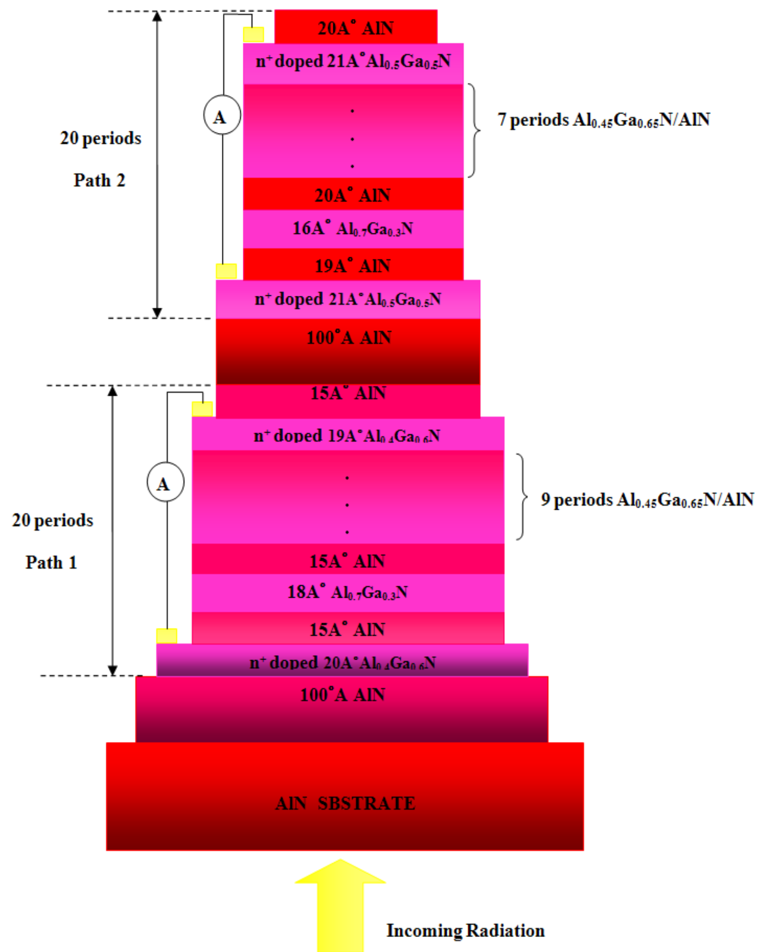

Figure 1. A 3D view of the design QCD with ability of detection 1.33 μm and 1.55 μm wavelengths in two separated paths.

Table 1. Path1 with 20 periods MQWs for detection 1.33 μm.

Wells	Thickness (Å)	Barriers	Thickness (Å)
$Al_{0.4}Ga_{0.6}N$	20	AlN	15
$Al_{0.7}Ga_{0.3}N$	18	AlN	16
$Al_{0.45}Ga_{0.45}N$	10	AlN	16
$Al_{0.45}Ga_{0.45}N$	11	AlN	16
$Al_{0.45}Ga_{0.45}N$	12	AlN	16
$Al_{0.45}Ga_{0.45}N$	13	AlN	16
$Al_{0.45}Ga_{0.45}N$	14	AlN	16
$Al_{0.45}Ga_{0.45}N$	15	AlN	16
$Al_{0.45}Ga_{0.45}N$	16	AlN	16
$Al_{0.45}Ga_{0.45}N$	17	AlN	16
$Al_{0.45}Ga_{0.45}N$	19	AlN	16
$Al_{0.4}Ga_{0.6}N$	20	AlN	16

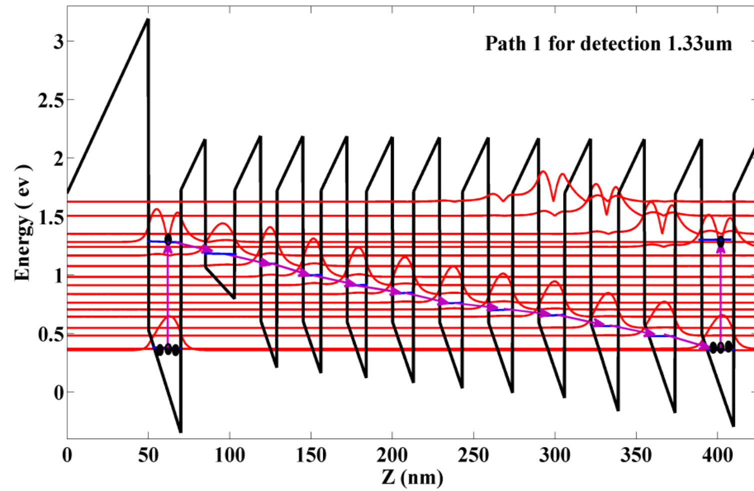

(a)

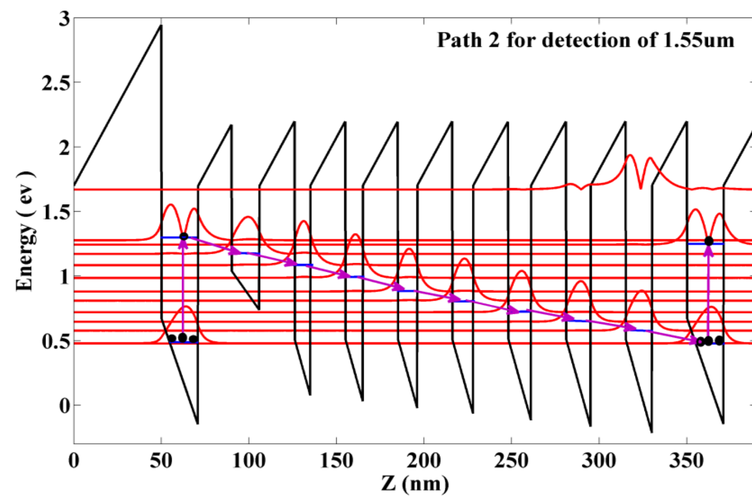

(b)

Figure 2. Conduction band edge and wave functions for each path for detection of (a) 1.33 μm and (b) 1.55 μm.

Table 2. Path 2 with 20 periods MQWs for detection 1.55 μm.

Wells	Thickness (Å)	Barriers	Thickness (Å)
$Al_{0.5}Ga_{0.5}N$	21	AlN	19
$Al_{0.7}Ga_{0.3}N$	16	AlN	20
$Al_{0.4}Ga_{0.6}N$	9	AlN	20
$Al_{0.4}Ga_{0.6}N$	10	AlN	20
$Al_{0.4}Ga_{0.6}N$	11	AlN	20
$Al_{0.4}Ga_{0.6}N$	12	AlN	20
$Al_{0.4}Ga_{0.6}N$	13	AlN	20
$Al_{0.4}Ga_{0.6}N$	14	AlN	20
$Al_{0.4}Ga_{0.6}N$	15	AlN	20
$Al_{0.5}Ga_{0.5}N$	21	AlN	20

The wave functions are calculated by solving 1-D Schrodinger-Poisson self consistently at 80 ˚K [16]. For conduction band edges calculation pyroelectric and piezoelectric polarization effects in III-Nitrid materials are considered [17]. Internal electric field due to polarization effects in j^{th} layer for a k layers quantum structures is obtained as Equation (1) [18]:

$$F_j = \frac{\sum_{k \neq j} \left(P_k - P_j \right) L_k / \varepsilon_k}{\varepsilon_j \sum_k L_k / \varepsilon_k} \tag{1}$$

where, j and k are the number of layers. L_k, P_k, P_j, ε_j and ε_k are the length of layers, the total polarization and permittivity of j_{th} and k_{th} layer, respectively.

The absorption coefficient is obtained as Equation (2) [10]:

$$\alpha(\omega) = \frac{\omega \mu c e^2}{n_r} \left| M_{fi} \right|^2 \frac{m^* k_B T}{Leff \, \pi \hbar^2} \ln \left\{ \frac{1 + \exp[\left(E_F - E_i \right) / k_B T]}{1 + \exp[\left(E_F - E_f \right) / k_B T]} \right\} \times \frac{\hbar / \tau_{in}}{\left(E_f - E_i - \hbar\omega \right)^2 + \left(\hbar / \tau_{in} \right)^2} \tag{2}$$

where, E_i and E_f, are the quantized energy levels for the initial and final states, respectively. M_{fi}, μ, c, L_{eff}, n_r and τ_{in} are dipole matrix element between initial and final states, the permeability, the speed of light in free space, the effective spatial extent of electrons in subbands, the refractive index and the intersubband relaxation time respectively. The absorption coefficient at 80˚K for each path is indicated in **Figure 3**.

Absorption coefficient is linked to dipole matrix element between initial and final states through Equation (2). As illustrated the path for detection of 1.55 µm has small absorption coefficient due to the small overlapping of wave functions between initial and first levels.

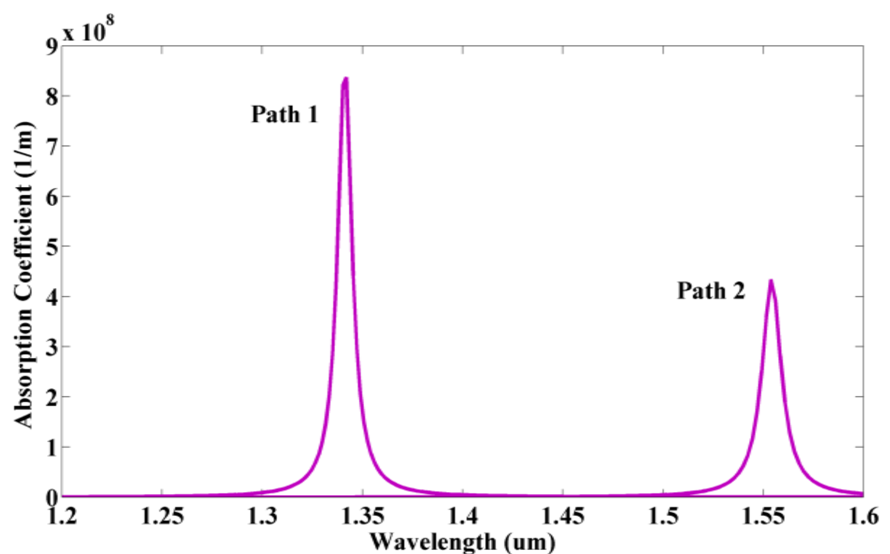

Figure 3. Absorption coefficient for paths versus incident wavelength at 80 ˚K.

The responsivity R for each path is obtained as Equation (3) [3]:

$$R = \eta \frac{\lambda q P_e}{N_{QW} hc P_c} \tag{3}$$

where, λ, c, q, h, η, P_e, P_c, N_{QW} are the incident wavelength, the speed of light in free space, the elementary charge, Planck's constant, the quantum efficiency, the escape probability of an excited electron in active QW, capture probability into the active QW's ground state for an electron traveling down the QCD's cascade and the number of active QW periods of the QCD. Absorption efficiency is expressed as Equation (4) [3]:

$$\eta = 1 - e^{-\alpha(\omega)d} \tag{4}$$

where, α and d are the absorption coefficient and thickness of active well in each period, respectively. The responsivity for each path at 80 ˚K is indicated in **Figure 4**.

In QCDs, resistance of the one period of the structure at zero bias in area of the device defined as R_0A, is an important parameter characterized the dark current (current in absence of incident light) [4]. In order to calculate the R_0A only interaction between electrons and LO-phonon is considered and interaction between electrons and acoustical phonons are neglected due to sufficient high differences between the energy levels in the studied structures [4]. R_0A is obtained as Equation (5) [4]:

$$R_0 A = \frac{k_B T}{q^2 \sum_{i \in A} \sum_{j \in B} G_{ij}} \tag{5}$$

Here, G_{ij} is global transition rate between the subband i and subband j and is the sum of the two transition rates for absorption of LO phonons (G_{aij}), and

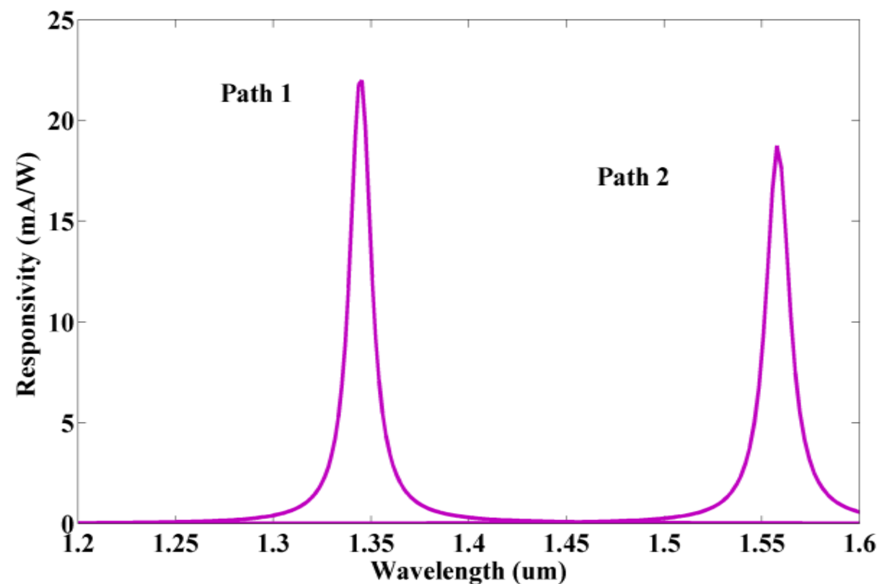

Figure 4. Responsivity for each path versus incident wavelength at 80 ˚K.

emission of LO phonons (G_{eij}) [4]. For one period of each path R_0A as a function of 1000/T is shown in **Figure 5**. To obtain the total resistance in area (R_0A) the values in **Figure 5** must be multiplied in numbers of periods. As shown in **Figure 5**, R_0A for path 1 has lower values than R_0A of path 2 due to higher transition rates values as described in the following. Dominant global transition rates between first energy level and other subbands in one period for paths are indicated in **Figure 6**.

Dominant transition rates values at temperatures of 80 ˚K, 120 ˚K and 240 ˚K for instances for paths 1 and 2 are listed in **Table 3** and **Table 4**, respectively.

As observed in **Table 3** and **Table 4** since global transition rates of path 1 are higher than the values for path 2 so, the resistance at null bias of path 1 is lower. Higher global transition rates between two levels can be related to higher overlapping of corresponding wave functions [3]. For path 1 this overlapping is high

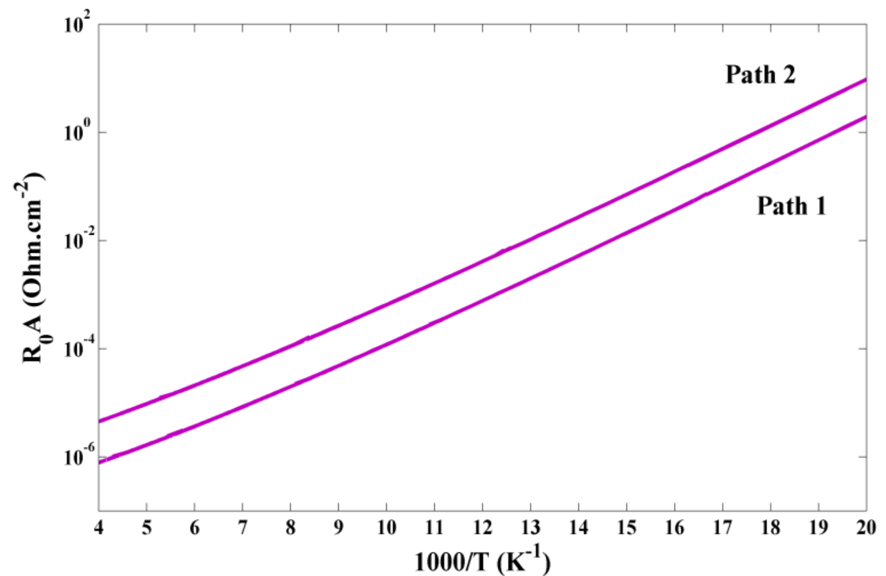

Figure 5. R_0A versus 1000/T (T is structure temperature).

Table 3. Dominant transition rates of path1 at three different temperatures.

Global transition rates ($m^{-2}\cdot s^{-1}$)	T = 80 ˚K	T = 120 ˚K	T = 240 ˚K
G_{112}	3.4559×10^{23}	2.3963×10^{25}	1.4414×10^{27}
G_{111}	1.3865×10^{20}	9.6905×10^{21}	5.9355×10^{23}
G_{110}	2.1841×10^{16}	1.5361×10^{18}	9.5414×10^{19}

Table 4. Dominant transition rates of path 2 at three different temperatures.

Global transition rates ($m^{-2}\cdot s^{-1}$)	T = 80 ˚K	T = 120 ˚K	T = 240 ˚K
G_{110}	5.9122×10^{22}	4.2822×10^{24}	2.4974×10^{26}
G_{19}	5.0429×10^{18}	3.5895×10^{20}	2.0865×10^{22}
G_{18}	1.0339×10^{14}	7.3362×10^{15}	4.2545×10^{17}

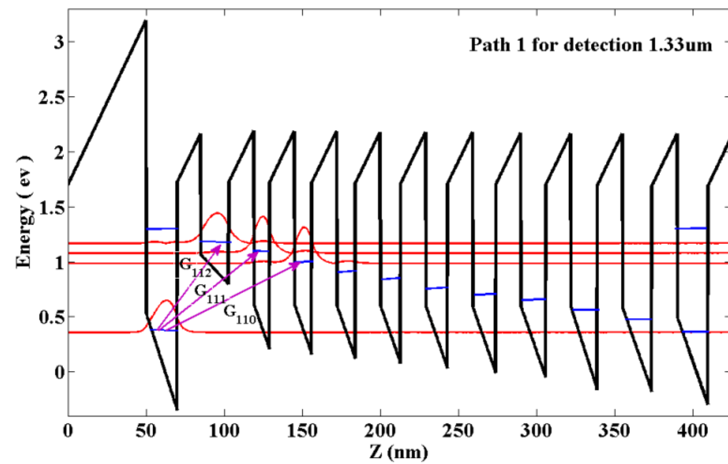

(a)

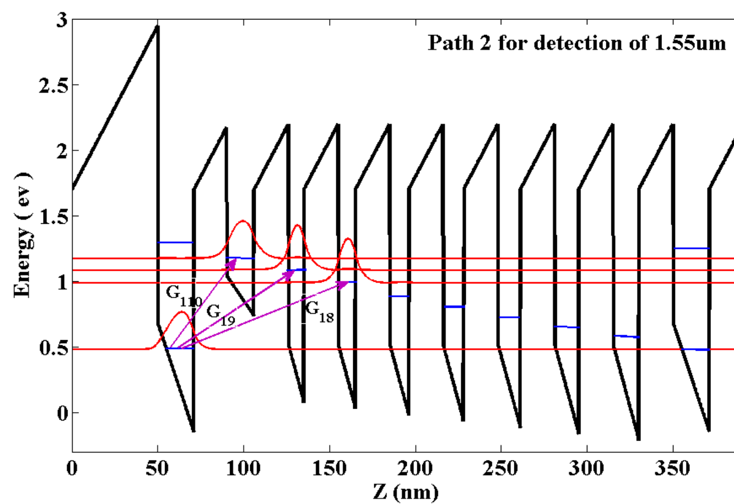

(b)

Figure 6. Dominant global transition rates for paths (a) 1 and (b) 2.

(due to having smaller width of the wells) which leads to smaller resistance values. Electron transition capability between two levels is increased by increasing temperature, therefore as shown in **Table 3** and **Table 4**, by increasing sample temperature the global rates is increased.

Detectivity for the designed detector is limited by Johnson-noise obtained as Equation 6 [3]:

$$D^{*} = R(\lambda)\sqrt{\frac{R_0 A}{4k_B T}} \tag{6}$$

where, $R(\lambda)$, R_0A are the responsivity spectrum and resistance of device in area of the device, respectively. Detectivity versus incident wavelength for paths at 80 ˚K is shown in **Figure 7**.

Paths have difference detectiveity values due to having different responsivity and resistivity (at zero bias) values shown in **Figure 4** and **Figure 5**, respectively.

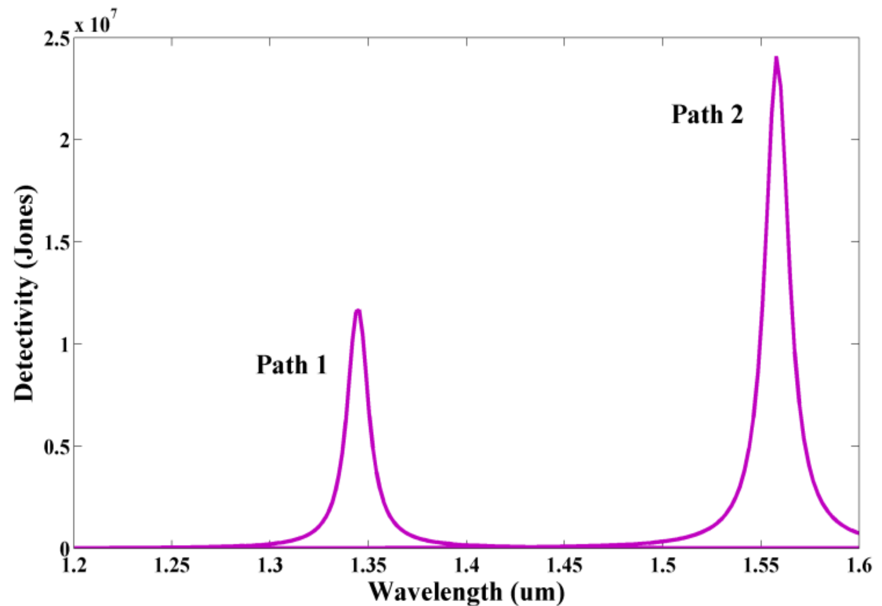

Figure 7. Detectivity spectrum for paths at 80 ˚K.

3. Conclusion

In this research, a QCD for detecting of 1.33 μm and 1.55 μm wavelengths in individual current paths based on intersubband transitions in AlGaN/AlN MQWs was designed. In order to calculate photodetector parameters, 1-D Schrodinger–Poisson equation self consistently at 80˚K was solved to obtain wave functions and energy levels. Responsivity values about 22 mA/W and 18.75 mA/W for detecting of 1.33 μm and 1.55 μm wavelengths, respectively. Detectivity values are calculated as 1.17×10^7 (Jones) and 2.41×10^7 (Jones) at wavelengths of 1.33 μm and 1.55 μm, respectively.

Acknowledgements

This work is supported by Photonics and Nanocrystal research Lab. (PNRL), Faculty of Electrical and Computer Engineering of Tabriz University and SP-EPT Labs., ASEPE Company, Industrial Park of Advanced Technologies, Tabriz, Iran.

References

[1] Dupont, E., Byloos, M., Gao, M., Buchanun, M., Song, C.Y., Wasilewski, Z.R. and Liu, H.C. (2002) Pixelless Thermal Imaging with Integrated Quantum Well Infrared Photodetector and Light Emitting Diode. *IEEE Photonics Technology Letters*, **14**, 182-184. https://doi.org/10.1109/68.980504

[2] Levine, B.F. (1993) Quantum Well Infrared Photodetectors. *J. Appl. Phys*, **74**, R1-R76. https://doi.org/10.1063/1.354252

[3] Giorgetta, F.R., Baumann, E., Graf, M., Yang, Q., Manz, C., Kohler, K., Beere, H.E., Ritchie, D.A., Linfield, E., Davies, A.G., Fedoryshyn, Y., Fischer, Jackel, H., Faist, J. and Hofstetter, D. (2009) Quantum Cascade Detectors. *IEEE Journal of Quantum*

Electronics, **8**, 1039-1052. https://doi.org/10.1109/JQE.2009.2017929

[4] Koeniguer, C., Dubois, G., Gomez, A. and Berger, V. (2006) Electronic Transport in Quantum Cascade Structures at Equilibrium. *Phys. Rev. B.*, **74**. https://doi.org/10.1103/PhysRevB.74.235325

[5] Rostami, A., Oliaee Rezayee, R., Rasooli Saghai, H., Yadipour, R. and Baghban, H. (2010) A Dual-Color IR Quantum Cascade Photodetector with Two Output Electrical Signals. *IEEE Transaction on Electron Devices,* **58**, 165-172. https://doi.org/10.1109/TED.2010.2082546

[6] Giorgetta, F.R., Baumann, E., Theron, R., Pellaton, M.L., Hofstetter, D., Fischer, M. and Faist, J. (2008) Short Wavelength (4μm) Quantum Cascade Detector Based on Strain Compensated InGaAs/InAlAs. *Appl. Phys. Lett*, **92**. https://doi.org/10.1063/1.2902301

[7] Graf, M., Hoyler, N., Giovannini, M., Faist, J. and Hofstetter, D. (2008) InP-Based Quantum Cascade Detectors in the Mid-Infrared. *Appl .Phys. Lett*, **88**.

[8] Giorgetta, F.R., Baumann, E., Graf, M., Ajili, L., Hoyler, N., Giovannini, M., Faist, J., Hofstetter, D., Krotz, P. and Sonnabend, G. (2007) 16.5 μm Quantum Cascade Detector Using Miniband Transport. *Appl .Phys. Lett*, **90**.

[9] Mei, T., Karunasiri, G. and Chua, S.J. (1997) Two-Color Infrared Detection Using Intersubband Transitions in Multiple Step Quantum Wells with Superlattice Barriers. *Appl. Phys. Lett.,* **71**.

[10] Ozturk, E. and Sokmen, I. (2003) Intersubband Transitions for Single, Double and Triple Si δ-Doped GaAs Layers. *Appl. Phys*, **36**. https://doi.org/10.1088/0022-3727/36/20/006

[11] Hofstetter, D., Baumann, E., Giorgetta, F.R., Theron, R., Wu, H., Schaff, W.J., Dawlaty, J., George, P.A., Eastman, L.F., Rana, F., Kandaswamy, P.K., Leconte, S. and Monroy, E. (2010) Intersubband Transition-Based Processes and Devices in AlN/GaN-Based Heterostructures. *Proceedings of the IEEE*, **7**. https://doi.org/10.1109/JPROC.2009.2035465

[12] Hofstetter, D., Baumann, E., Giorgetta, F.R., Theron, R., Wu, H., Schaff, W.J., Dawlaty, J., George, P.A., Eastman, L.F., Rana, F., Kandaswamy, P.K., Leconte, S. and Monroy, E. (2009) Photodetectors Based on Intersubband Transitions Using III-Nitride Superlattice Structures. *J. Phys.: Condens. Matter*, **21**. https://doi.org/10.1088/0953-8984/21/17/174208

[13] Zhanga, S.K., Wang, W.B., Yun, F., He, L., Morkoc, H., Zhou, X., Tamargo, M. and Alfano, R.R. (2002) Backilluminated Ultraviolet Photodetector Based on GaN/AlGaN Multiple Quantum Wells. *Appl. Phys. Lett*, **24**. https://doi.org/10.1063/1.1527994

[14] Teke, A., Dogan, S., Yun, F., Reshchikov, M.A., Le, H., Liu, X.Q., Morkoc, H., Zhang, S.K., Wang, W.B. and Alfano, R.R. (2003) GaN/AlGaN Back-Illuminated Multiple-Quantum-Well Schottky Barrier Ultraviolet Photodetectors. *Solid-State Electronics*, **47**. https://doi.org/10.1016/S0038-1101(03)00068-6

[15] Chen, G., Wang, X.Q., Rong, X., Wang, P., Xu, F.J., Tang, N., Qin, Z.X., Chen, Y.H. and Shen, B. (2015) Intersubband Transition in GaN/InGaN Multiple Quantum Wells. *Nature*, *Science Report*.

[16] Rostami, A., Baghban, H. and Rasooli Saghai, H. (2007) An Ultra-High Level Second-Order Nonlinear Optical Susceptibility in Strained Asymmetric GaN-AlGaN-AlN Quantum Wells: Towards All-Optical Devices and Systems. *Microelectronics Journal*, **38**, 900-904. https://doi.org/10.1016/j.mejo.2007.07.071

[17] Galczak, J., SarzaLa, R.P. and Nakwaski, W. (2004) Spatial Separation of Recom-

bining Carriers within Nitride GaN/(AlGa)N Quantum Wells Induced by Piezoelectric Phenomena. *Opto-Eelectron. Rev.*, **12**, 369.

[18] Li, Y. and Paiella, R. (2006) Intersubband All-Optical Switching Based on Coulomb-Induced Optical Nonlinearities in GaN/AlGaN. *Semicond. Sci. Technol.*, **21**, 1105. https://doi.org/10.1088/0268-1242/21/8/022

Submit or recommend next manuscript to SCIRP and we will provide best service for you:

Accepting pre-submission inquiries through Email, Facebook, LinkedIn, Twitter, etc.
A wide selection of journals (inclusive of 9 subjects, more than 200 journals)
Providing 24-hour high-quality service
User-friendly online submission system
Fair and swift peer-review system
Efficient typesetting and proofreading procedure
Display of the result of downloads and visits, as well as the number of cited articles
Maximum dissemination of your research work

Submit your manuscript at: http://papersubmission.scirp.org/
Or contact opj@scirp.org